

Numerical Heat Transfer, Part A: Applications

An International Journal of Computation and Methodology

ISSN: 1040-7782 (Print) 1521-0634 (Online) Journal homepage: <https://www.tandfonline.com/loi/unht20>

Modeling of indoor airflow around thermal manikins by multiple-relaxation-time lattice Boltzmann method with LES approaches

Xiaojie Cheng, Ruoyu Su, Xiong Shen, Tingxuan Deng, Delun Zhang, Di Chang, Boyue Zhang & Shanshan Qiu

To cite this article: Xiaojie Cheng, Ruoyu Su, Xiong Shen, Tingxuan Deng, Delun Zhang, Di Chang, Boyue Zhang & Shanshan Qiu (2020) Modeling of indoor airflow around thermal manikins by multiple-relaxation-time lattice Boltzmann method with LES approaches, Numerical Heat Transfer, Part A: Applications, 77:2, 215-231, DOI: [10.1080/10407782.2019.1685822](https://doi.org/10.1080/10407782.2019.1685822)

To link to this article: <https://doi.org/10.1080/10407782.2019.1685822>



Published online: 03 Dec 2019.



Submit your article to this journal [↗](#)



Article views: 47



View related articles [↗](#)



View Crossmark data [↗](#)



Modeling of indoor airflow around thermal manikins by multiple-relaxation-time lattice Boltzmann method with LES approaches

Xiaojie Cheng, Ruoyu Su, Xiong Shen, Tingxuan Deng, Delun Zhang, Di Chang, Boyue Zhang, and Shanshan Qiu

Tianjin Key Lab of Indoor Air Environmental Quality Control, School of Environmental Science and Engineering, Tianjin University, P.R. China

ABSTRACT

As an effective CFD approach, Multiple-Relaxation-Time Lattice Boltzmann Method (MRT-LBM) has gradually gained its popularity in the past 20 years. In this article, a case that simulated the airflow patterns surrounding the human bodies were studied using MRT-LBM. The governing equation was solved by the MRT-LBM in the simulation. In order to calculate the boundary layer around the complicated geometry, wall-adapting local eddy viscosity (WALE) model was applied for the turbulence model. The D3Q19 and D3Q7 models were applied for the discretization of momentum and energy equation, respectively. In order to analyze the grid independence, three lattice densities were compared in this study. The simulation results were compared with the finite volume method (FVM) as well as the experimental data. Results showed that MRT-LBM with grid resolution of 0.01 m would obtain accurate results of airflow surrounding the human bodies. FVM required 5–6 times computation time than the MRT-LBM. Thereby, the MRT-LBM method can have advantages in the indoor airflow simulation field especially when the indoor geometry is complicated.

ARTICLE HISTORY

Received 24 June 2019

Accepted 23 October 2019

1. Introduction

Human spends more than 80 percent of life in indoor environment [1]. In order to design a healthy indoor air environment, it is very important to establish an accurate prediction method. As for indoor environment, the human bodies interact closely with their surroundings by serving as obstacles of airflow, source and sink of various contaminants and the major heat source of thermal buoyancy flows [2]. Therefore, it is crucial to consider the human factors when predicting the indoor airflow.

At least 50 years ago, thermal manikins had been introduced and widely applied to simulate the human bodies in the indoor environment [3]. As the thermal manikins became closer to the human bodies, researchers can obtain data about indoor velocity, temperature and pollutant transportation by laboratory experiments [4, 5]. However, the cost of the experiment is usually high. It is also very difficult to acquire comprehensive data of airflow field through the experiments.

With the development of computers, CFD was applied to simulate the airflow around the thermal manikins in the past twenty years. Gao and Niu [6] simulated the airflow field surrounding a seated manikin. Topp et al. [7] and Topp [8] studied the effect of using different manikin models such as a

Nomenclature

e_α	discrete velocities	$p_{xy,yz,zz,zz}$	
S, Q	collision matrix	p_{xx}, p_{yy}, p_{zz}	symmetric traceless viscous stress tensor
m_α	moments	$m_{x,y,z}$	cubic order
r_i	lattice nodes	$\pi_{x,y,z}$	quartic order
m_α^{eq}	equilibrium value of the moments m_α	M, N	transformation matrix
ρ	mass density	τ_{ij}	relaxation coefficient
e	kinetic energy	δ_{ij}	Kronecker's delta
ε	kinetic energy square	ν_0	molecular viscosity
τ_{ij}	SGS stress term	Δ	cutoff length
ν_t	turbulent viscosity		
$j_{x,y,z}$	momentum		
$q_{x,y,z}$	energy flux		

complete and a simplified geometry. They found that the geometry had large influence on the flow region close to the manikins. Keshavarz et al [9] investigated the effect of manikin's thermal plume, motion and breathing on indoor air quality using CFD approach. CFD has the advantage of obtaining detailed airflow information surrounding the manikins. However, because the geometry of the manikins was quite complicated, the process of mesh generation as well as the computation iterations requires massive time and computer resources. Thereby, many scientists have been inclined to apply simplified geometry even though it may cause inaccuracies [7, 8].

The error of CFD simulation may come from the computation meshes in terms of grid size and distribution. Martinho et al. [10] evaluated the errors of CFD in simulating airflow and heat transfer through and around a thermal manikin. They found the optimal grid resolution surrounding the manikins has an initial height of 0.5 mm and an expansion ratio of 1.15.

The above-mentioned studies applied Finite Volume Method (FVM) to solve the Navier–Stokes equations for the indoor airflow prediction. In the past two decades, a different CFD method namely Lattice Boltzmann Method (LBM) had been applied in many fields [11–15]. Different from FVM and N-S, the LBM solves the discrete Boltzmann equation by modeling fluids at the so-called mesoscopic level [16]. In discrete Boltzmann equation, the kinetic equation is solved by the density distribution function of fictitious particles. The variables such as velocity and pressure are obtained by evaluating the moments of the particle distribution function [17]. LBM has shown its advantage in predicting turbulent flow [18, 19]. LBM has two commonly applied forms such as lattice BGK equations and MRT-LBM. The lattice BGK equation was very popular because it has the very simple form; however, its deficiencies were large [20]. The MRT-LBM overcomes some obvious defects of the lattice BGK model in which the relaxation time cannot be individually tuned to achieve optimal stability. Results also showed that the MRT-LBM model was more stable and suitable in resolving high-Reynolds flow conditions than lattice BGK as presented in [21].

Encouraged by above researches, we started to apply the MRT-LBM approach in predicting indoor airflow by thermal manikins. Because the geometry of manikins was complicated, we optimized grid distributions surrounding the manikins. We also compared with FVM by the experimental data in order to analyze the accuracy and the computation cost.

2. Numerical methods

2.1 Multiple-relaxation-time lattice Boltzmann method

Boltzmann equation, also called the Boltzmann transport equation, is an equation describes the statistical distribution of particles in fluid. In Boltzmann equation, the particle distribution function $f(\mathbf{r}, \mathbf{e}, t)$ is evolved in the phase space, in which \mathbf{r} , \mathbf{e} , and t represent the particle position,

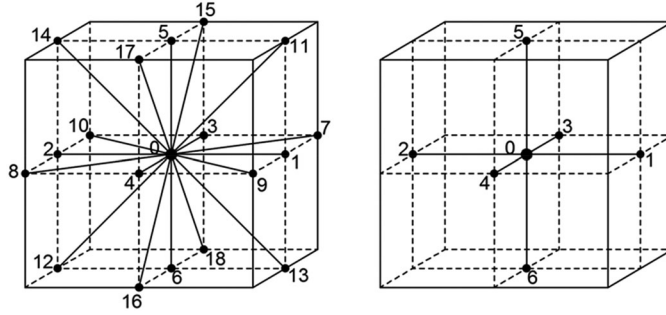


Figure 1. D3Q19 and D3Q7 model: 0-18, 0-6 are the discrete velocities.

particle velocity and time. With the distribution function, the density of a particular molecule at a given position and the momentum can be obtained.

In order to achieve more flexible and reliable solutions, scientists have proposed a new method named MRT LBM method. It uses maximum freedom in the construction of the equilibrium functions of the non-conserved moments [20]. Lallemand and Luo [21] showed that the MRT LBM model has high stability. The evolution equation for MRT LBM can be described as follows:

$$\left| f(\mathbf{r}_i + \mathbf{e}_\alpha \delta_t, t + \delta_t) - \right| f(\mathbf{r}_i, t) = -M^{-1} \cdot \mathbf{S} \cdot \left[m(\mathbf{r}_i, t) - m^{\text{eq}}(\mathbf{r}_i, t) \right] \quad (1)$$

where \mathbf{e}_α are discrete velocities, \mathbf{S} is the collision matrix, and m_α are the moments obtained from distribution functions f_α , $m_\alpha = f | \Phi_\alpha = \Phi_\alpha | f$.

where Φ_α are the Q orthogonal basis vectors. $| \cdot$ represents column vectors, $\cdot |$ represents row vectors, \mathbf{r}_i represents the lattice nodes, and m_α^{eq} is the equilibrium value of the moments m_α . In Equation (1), the left and right side represent the streaming and collision step, respectively.

2.2. Spatial and numerical discretization

The commonly applied spatial discretization method was proposed by Qian et al. [20]. The method named DnQm model, in which Dn means n-dimensional space and Qm means m-discrete direction as shown in Figure 1. The challenge of this method is to couple the energy and momentum terms in a single LBM equation. There were two common ways for the coupling. One is to obtain the temperature field by adding more discrete velocities to the particle density distribution [22]. Lallemand and Luo found that this might lead to defects such as numerical instability and spurious mode coupling [23]. By applying more discrete velocities in one model, the range of temperature variation must be small and the numerical instability was inevitable [24]. Another method is to solve the temperature field by other numerical methods such as finite element method and Monte Carlo method. This may have an advantage in the stability but may acquire massive computational resources. In order to deal with the instability problems, the optimal method in LBM is not to couple the energy and momentum terms in one DnQm model but separately. In this study, the model namely double MRT model was applied. The double MRT model applied D3Q19 model for flow field and D3Q7 model for thermal field.

2.2.1. D3Q19 model for velocity field

In the LBM simulation, the computational domain was discretized into massive lattices. Each lattice node has 19 discrete velocities. As shown in Figure 1, the MRT D3Q19 model for the velocity field contained 19 discrete velocities \mathbf{e}_α [25]:

$$\mathbf{e}_\alpha = \begin{cases} (0,0,0), & \alpha = 0 \\ (\pm 1, 0, 0) (0, \pm 1, 0) (0, 0, \pm 1), & \alpha = 1, 2, \dots, 6 \\ (\pm 1, \pm 1, 0) (\pm 1, \pm 1, \pm 1) (\pm 1, 0, \pm 1), & \alpha = 7, 8, \dots, 18 \end{cases} \quad (2)$$

For the MRT LBM evolution equation, the 19 moments in Equation (3) are

$$|\mathbf{m}\rangle = (\rho, e, \varepsilon, j_x, q_x, j_y, q_y, j_z, q_z, 3p_{xx}, 3\pi_{xx}, p_{ww}, \pi_{ww}, p_{xy}, p_{yz}, p_{xz}, m_x, m_y, m_z)^T \quad (3)$$

where ρ is the mass density, e is the kinetic energy independent of the density, ε is the kinetic energy square independent of the density and kinetic energy, $j_{x,y,z}$ is the momentum, $q_{x,y,z}$ is the energy flux independent of the mass flux, $p_{xy,yz,zx}$, p_{xx} , and p_{ww} are the symmetric traceless viscous stress tensor, $m_{x,y,z}$ is the cubic order and $\pi_{x,y,z}$ is the quartic order.

The collision is executed in the moment space $\mathbf{W} = \mathbf{R}^Q$, while the advection is performed in the velocity space $\mathbf{V} = \mathbf{R}^Q$. The moment space \mathbf{W} spanned by $|\mathbf{m}\rangle$ are related by a transformation matrix \mathbf{M} : $|\mathbf{m}\rangle = \mathbf{M}|\mathbf{f}\rangle$ and $|\mathbf{f}\rangle = \mathbf{M}^{-1}|\mathbf{m}\rangle$. The transformation matrix \mathbf{M} is

$$\mathbf{M} = \begin{bmatrix} 1 & 1 & 1 & 1 & 1 & 1 & 1 & 1 & 1 & 1 & 1 & 1 & 1 & 1 & 1 & 1 & 1 & 1 \\ -30 & -11 & -11 & -11 & -11 & -11 & -11 & 8 & 8 & 8 & 8 & 8 & 8 & 8 & 8 & 8 & 8 & 8 \\ 12 & -4 & -4 & -4 & -4 & -4 & -4 & 1 & 1 & 1 & 1 & 1 & 1 & 1 & 1 & 1 & 1 & 1 \\ 0 & 1 & -1 & 0 & 0 & 0 & 0 & 1 & -1 & 1 & -1 & 1 & -1 & 1 & -1 & 0 & 0 & 0 \\ 0 & -4 & 4 & 0 & 0 & 0 & 0 & 1 & -1 & 1 & -1 & 1 & -1 & 1 & -1 & 0 & 0 & 0 \\ 0 & 0 & 0 & 1 & -1 & 0 & 0 & 1 & 1 & -1 & -1 & 0 & 0 & 0 & 0 & 1 & -1 & 1 & -1 \\ 0 & 0 & 0 & -4 & 4 & 0 & 0 & 1 & 1 & -1 & -1 & 0 & 0 & 0 & 0 & 1 & -1 & 1 & -1 \\ 0 & 0 & 0 & 0 & 0 & 1 & -1 & 0 & 0 & 0 & 0 & 1 & 1 & -1 & -1 & 1 & 1 & -1 & -1 \\ 0 & 0 & 0 & 0 & 0 & -4 & 4 & 0 & 0 & 0 & 0 & 1 & 1 & -1 & -1 & 1 & 1 & -1 & -1 \\ 0 & 2 & 2 & -1 & -1 & -1 & -1 & 1 & 1 & 1 & 1 & 1 & 1 & 1 & 1 & -2 & -2 & -2 & -2 \\ 0 & -4 & -4 & 2 & 2 & 2 & 2 & 1 & 1 & 1 & 1 & 1 & 1 & 1 & 1 & -2 & -2 & -2 & -2 \\ 0 & 0 & 0 & 1 & 1 & -1 & -1 & 1 & 1 & 1 & 1 & -1 & -1 & -1 & -1 & 0 & 0 & 0 & 0 \\ 0 & 0 & 0 & -2 & -2 & 2 & 2 & 1 & 1 & 1 & 1 & -1 & -1 & -1 & -1 & 0 & 0 & 0 & 0 \\ 0 & 0 & 0 & 0 & 0 & 0 & 0 & 1 & -1 & 1 & -1 & 0 & 0 & 0 & 0 & 0 & 0 & 0 & 0 \\ 0 & 0 & 0 & 0 & 0 & 0 & 0 & 0 & 0 & 0 & 0 & 0 & 0 & 0 & 0 & 1 & -1 & -1 & 1 \\ 0 & 0 & 0 & 0 & 0 & 0 & 0 & 0 & 0 & 0 & 0 & 1 & -1 & -1 & 1 & 0 & 0 & 0 & 0 \\ 0 & 0 & 0 & 0 & 0 & 0 & 0 & 1 & -1 & 1 & -1 & -1 & 1 & -1 & 1 & 0 & 0 & 0 & 0 \\ 0 & 0 & 0 & 0 & 0 & 0 & 0 & -1 & -1 & 1 & 1 & 0 & 0 & 0 & 0 & 1 & -1 & 1 & -1 \\ 0 & 0 & 0 & 0 & 0 & 0 & 0 & 0 & 0 & 0 & 0 & 1 & 1 & 1 & -1 & -1 & -1 & 1 & 1 \end{bmatrix} \quad (4)$$

With $C_s^2 = 1/3$ and $s_9 = s_{13}$, the equilibrium moments can be given as

$$|\mathbf{m}^{\text{eq}}\rangle = [m_0^{\text{eq}}, m_1^{\text{eq}}, m_2^{\text{eq}}, m_3^{\text{eq}}, m_4^{\text{eq}}, m_5^{\text{eq}}, m_6^{\text{eq}}, m_7^{\text{eq}}, m_8^{\text{eq}}, m_9^{\text{eq}}, m_{10}^{\text{eq}}, m_{11}^{\text{eq}}, m_{12}^{\text{eq}}, m_{13}^{\text{eq}}, m_{14}^{\text{eq}}, m_{15}^{\text{eq}}, m_{16}^{\text{eq}}, m_{17}^{\text{eq}}, m_{18}^{\text{eq}}]^T \quad (5)$$

Where the equilibrium moments 0–18 was given as

$$\begin{aligned} m_0^{\text{eq}} &= \rho, \quad m_1^{\text{eq}} = -11\rho + 19\frac{j_x^2 + j_y^2 + j_z^2}{\rho_0}, \quad m_2^{\text{eq}} = 3\rho - \frac{11j_x^2 + j_y^2 + j_z^2}{2\rho_0} \\ m_3^{\text{eq}} &= j_x, \quad m_4^{\text{eq}} = -\frac{2}{3}j_x, \quad m_5^{\text{eq}} = j_y, \quad m_6^{\text{eq}} = -\frac{2}{3}j_y, \quad m_7^{\text{eq}} = j_z, \quad m_8^{\text{eq}} = -\frac{2}{3}j_z \\ m_9^{\text{eq}} &= \frac{2j_x^2 - (j_y^2 + j_z^2)}{\rho_0}, \quad m_{10}^{\text{eq}} = -\frac{2j_x^2 - (j_y^2 + j_z^2)}{2\rho_0} \\ m_{11}^{\text{eq}} &= \frac{j_y^2 - j_z^2}{\rho_0}, \quad m_{12}^{\text{eq}} = -\frac{j_y^2 - j_z^2}{2\rho_0}, \quad m_{13}^{\text{eq}} = \frac{j_x j_y}{\rho_0}, \quad m_{14}^{\text{eq}} = \frac{j_y j_z}{\rho_0}, \quad m_{15}^{\text{eq}} = \frac{j_x j_z}{\rho_0} \\ m_{16,17,18}^{\text{eq}} &= 0 \end{aligned}$$

where

$$\rho = \sum_{i=1}^{19} f(r_i, t), \quad j_x = \rho e_x, \quad j_y = \rho e_y, \quad j_z = \rho e_z \quad (6)$$

where \mathbf{S} is the diagonal collision matrix:

$$\mathbf{S} = \text{diag}(0, s_1, s_2, 0, s_4, 0, s_4, 0, s_4, s_9, s_{10}, s_9, s_{10}, s_{13}, s_{13}, s_{13}, s_{16}, s_{16}, s_{16}) \quad (7)$$

2.2.2. D3Q7 for thermal field

We applied the D3Q7 model to resolve the anisotropic diffusion and convection equation in the energy equation of MRT LBM (Equation (1)) as proposed by Yoshida and Nagaoka [26]. The D3Q7 model has shown high efficiency and accuracy in the numerical discretization of energy terms [26]. As shown in Figure 1, the seven discrete velocities \mathbf{e}_α was calculated as

$$\mathbf{e}_\alpha = \begin{cases} (0, 0, 0), & \alpha = 0 \\ (\pm 1, 0, 0) & (0, \pm 1, 0) & (0, 0, \pm 1), & \alpha = 1, 2, \dots, 6 \end{cases} \quad (8)$$

Based on the D3Q7 model, the distribution function in Equation (1) of energy g_i changed into

$$|g(\mathbf{r}_i + \mathbf{e}_\alpha \delta t, t + \sigma t) - |g(\mathbf{r}_i, t) = -N^{-1} \mathbf{Q} [|n(\mathbf{r}_i, t) - |n^{\text{eq}}(\mathbf{r}_i, t)] \quad (9)$$

where (\mathbf{r}_i, t) is the corresponding moments of $g(\mathbf{r}_i, t)$, $|n = N|g$ and $|g = N^{-1}|n$. $n^{\text{eq}}(\mathbf{r}_i, t)$ are the equilibrium moments for $n(\mathbf{r}_i, t)$,

$$|n^{\text{eq}}\rangle = [T, e_x T, e_y T, e_z T, aT, 0, 0]^T \quad (10)$$

where a is a constant. The macroscopic parameters T can be obtained by

$$T = \sum_{i=1}^7 g(\mathbf{r}_i, t) \quad (11)$$

where N is the transformation matrix for the energy distribution function, \mathbf{Q} is the collision matrix. Matrix N and \mathbf{Q} are

$$N = \begin{bmatrix} 1 & 1 & 1 & 1 & 1 & 1 & 1 \\ 0 & 1 & -1 & 0 & 0 & 0 & 0 \\ 0 & 0 & 0 & 1 & -1 & 0 & 0 \\ 0 & 0 & 0 & 0 & 0 & 1 & -1 \\ 6 & -1 & -1 & -1 & -1 & -1 & -1 \\ 0 & 2 & 2 & -1 & -1 & -1 & -1 \\ 0 & 0 & 0 & 1 & 1 & -1 & -1 \end{bmatrix} \quad \mathbf{Q}^{-1} = \begin{bmatrix} \tau_0 & 0 & 0 & 0 & 0 & 0 & 0 \\ 0 & \bar{\tau}_{xx} & \bar{\tau}_{xy} & \bar{\tau}_{xz} & 0 & 0 & 0 \\ 0 & \bar{\tau}_{xy} & \bar{\tau}_{yy} & \bar{\tau}_{yz} & 0 & 0 & 0 \\ 0 & \bar{\tau}_{xz} & \bar{\tau}_{yz} & \bar{\tau}_{zz} & 0 & 0 & 0 \\ 0 & 0 & 0 & 0 & \tau_4 & 0 & 0 \\ 0 & 0 & 0 & 0 & 0 & \tau_5 & 0 \\ 0 & 0 & 0 & 0 & 0 & 0 & \tau_6 \end{bmatrix} \quad (12)$$

Where $\bar{\tau}_{ij}$ is the relaxation coefficient, δ_{ij} is the Kronecker's delta.

$$\bar{\tau}_{ij} = \frac{1}{2} \delta_{ij} + \frac{\delta t}{\varepsilon \delta r^2} D_{ij} \quad \delta_{ij} = \begin{cases} 0 & \text{if } i \neq j \\ 1 & \text{if } i = j \end{cases} \quad (13)$$

2.3. Turbulence model

In this study, we applied LES approaches to resolve the velocity and temperature among lattices. We applied the wall-adapting local eddy viscosity (WALE) sub-grid scale model proposed by Ducros et al. [27] in this article. The WALE model is suitable to solve the asymptotic flow in the turbulent boundary layer and appropriate for complicated boundaries.

$$\partial \frac{\bar{u}_i}{\partial x_i} = 0 \quad (14)$$

$$\partial \frac{\bar{u}_i}{\partial t} + \bar{u}_j \frac{\partial \bar{u}_i}{\partial x_j} = -\frac{1}{\rho} \partial \frac{\bar{p}}{\partial x_i} + \frac{\partial}{\partial x_j} \left(\nu \frac{\partial \bar{u}_i}{\partial x_j} \right) + \frac{\partial \tau_{ij}}{\partial x_j} \quad (15)$$

$$\tau_{ij} = \bar{u}_i \bar{u}_j - \overline{u_i u_j} \quad (16)$$

τ_{ij} is the SGS stress term, which can be calculated by:

$$\tau_{ij} = -\frac{1}{3} \tau_{kk} \delta_{ij} = -2\nu_t \bar{S}_{ij} \quad (17)$$

For LES, $\nu = \nu_0 + \nu_t$, where ν_0 and ν_t are the molecular viscosity and turbulent viscosity, respectively. WLES defined a new operator based on the traceless symmetric part of the square of the gradient velocity tensor, which solves the turbulence viscosity ν_t by [23]

$$\nu_t = (C_m \Delta)^2 \frac{(S_{ij}^d S_{ij}^d)^{3/2}}{(\bar{S}_{ij} \bar{S}_{ij})^{5/2} + (S_{ij}^d S_{ij}^d)^{5/4}} \quad (18)$$

where, Δ is the cutoff length, in this study, which equal to the lattice size. \bar{S}_{ij} is the symmetric part of the velocity gradient \bar{g}_{ij}

$$\bar{S}_{ij} = \frac{1}{2} (\bar{g}_{ij} + \bar{g}_{ji}), \quad \bar{g}_{ij} = \partial \frac{\bar{u}_i}{\partial x_j}, \quad \text{and} \quad \bar{g}_{ji} = \partial \frac{\bar{u}_j}{\partial x_i} \quad (19)$$

S_{ij}^d is an operator based on the traceless symmetric part of the square of \bar{g}_{ij}

$$S_{ij}^d = \frac{1}{2} (\bar{g}_{ij}^2 + \bar{g}_{ji}^2) - \frac{1}{3} \delta_{ij} \bar{g}_{kk}^2 \quad (20)$$

C_m is a constant obtained by

$$C_m^2 = C_s^2 \sqrt{2} \left(\frac{\bar{S}_{ij} \bar{S}_{ij}}{\psi(S_{ij}^d S_{ij}^d) \bar{S}_{ij} \bar{S}_{ij}} \right)^2 \quad (21)$$

2.4. Boundary condition setup

We used the continuous bounce-back (CBB) boundary condition proposed by Verberg and Ladd [28] in this study. CBB was derived from the classical link bounce-back (LBB) boundary condition. The latter has difficulty in acquiring the shape information of the particle surface, especially in complicated boundary conditions. CBB resolves the density distribution, $f(\mathbf{r}, \mathbf{e}, t)$ or $g(\mathbf{r}, \mathbf{e}, t)$ by considering the reflections throughout partially filled cells at the solid-fluid interface. The basic formula of CBB rules of velocity distribution functions at the interface is:

$$f_i^*(\mathbf{r}, t) = f_i(\mathbf{r}, t) + \Delta_i [f(\mathbf{r}, t)] + g_i(\mathbf{r}, t) \quad (22)$$

$$f_i^*(\mathbf{r}, t) = f_i(\mathbf{r} + \mathbf{c}_i, t + 1) \quad (23)$$

where $f(\mathbf{r}, t)$ the velocity distribution functions, $f^*(\mathbf{r}, t)$ are the post-collision distributions, Δ_i the collision operator, and $g(\mathbf{r}, t)$ is the effect of external forces.

Assumed that the density distribution changes linearly in the direction of lattice connection, Equation (22) becomes

$$f_i^*(\mathbf{x}, t) = \frac{2\mathbf{x}}{1 + \beta} [f_i^*(\mathbf{r}_2, t) - f_i^*(\mathbf{r}_1, t)] + f_i^*(\mathbf{r}_1, t) \quad (24)$$

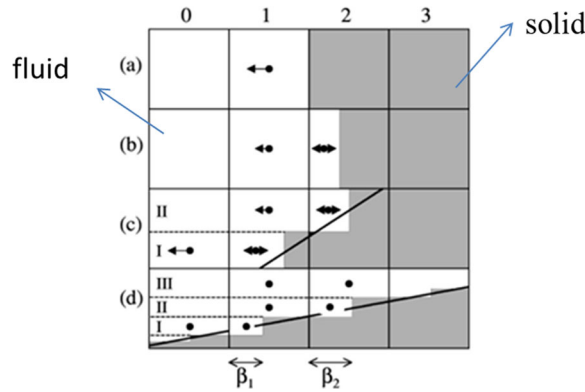


Figure 2. Schematic representation of the solid and fluid boundary with different geometries in CBB [29].

where β is an independent variable between 0 and 1 according to the proportion of the solid part and the fluid part occupied in the grid, x is the distance between the interface of cell 1 and 2. i is the label of lattices.

The CBB was described in a two-dimensional case as shown in Figure 2: Firstly, the LBM divided the 2D computational domain into multiple lattices with equal area. It is obvious that part of the lattice boundary coincides with the solid boundary, such as (a), while partly boundaries do not coincide with the solid boundary, such as (b, c, d). At that time, β are different from varied lattices, as seen in the literature [30]. In Figure 2, the solid dots indicate the location of the mean population density in each cell or part of a cell, and the solid arrows indicate the propagation of population densities of $f_i^*(\mathbf{r}_i, t)$. The double sided arrow indicates the population densities $f_1(\mathbf{r}_i, t)$ and $f_2(\mathbf{r}_i, t)$ are moving to the right and left, respectively. The bold lines in (c) and (d) indicate an inclined boundary with solid and fluid boundary mixed in the boundary lattices. Each lattice treated the inclined boundary by partially filling the mixed lattice in sequence. Because the CBB can treat the lattices surround the interface in those four manners (a, b, c, d), therefore, it is very suitable for arbitrarily complex computational domain with complicated boundaries.

3. Benchmark test

3.1. Benchmark test

In order to validate the MRT LBM, we applied the result of a benchmark test with a mixing ventilation case by Nielsen et al. [31]. The benchmark test applied a seated thermal manikin in the experiment as shown in Figure 3. It has been widely applied to validate the CFD tools [6–8, 10, 30, 32].

Those studies applied a Computer Simulated Person (CSP) as geometry. As seen in Figure 3, the female manikin model was proposed by Kato's research group, which was created using stereo-lithographic technique, namely a 3-D printing method using liquid photosensitive resin. The manikin was located in the experimental room. The room had a size of 1.2 m wide, 2.44 m long and 2.46 m high. The inlet was the front opening surface and two exhaust outlets were located at the backward wall. The diameter of the exhaust opening was 0.25 m. The inlet air had a mean velocity of 0.2 m/s and a mean temperature of 22 °C. Radiation effect was not considered in the experiment. The measured velocities at nine sampled lines (lines 1–9) in the benchmark test were applied for the validation as seen in Figure 3.

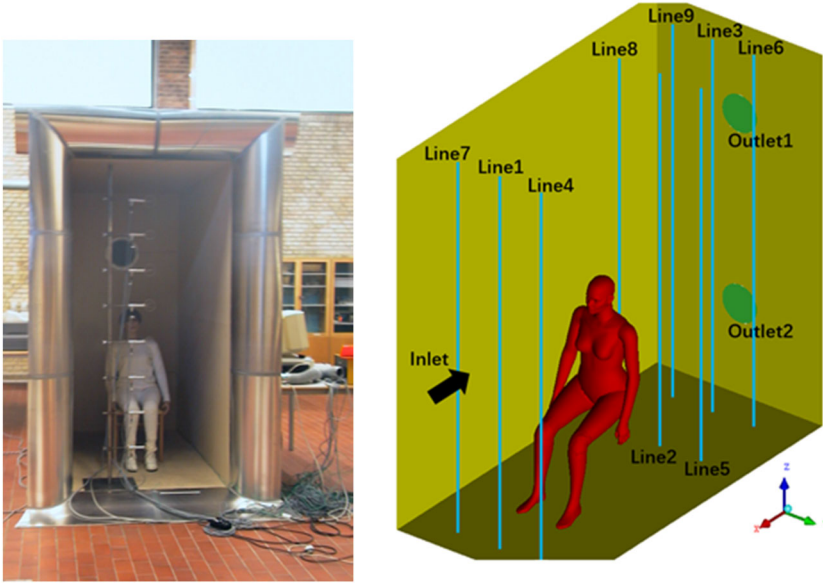


Figure 3. Experiment setup of the mixing ventilated room [31].

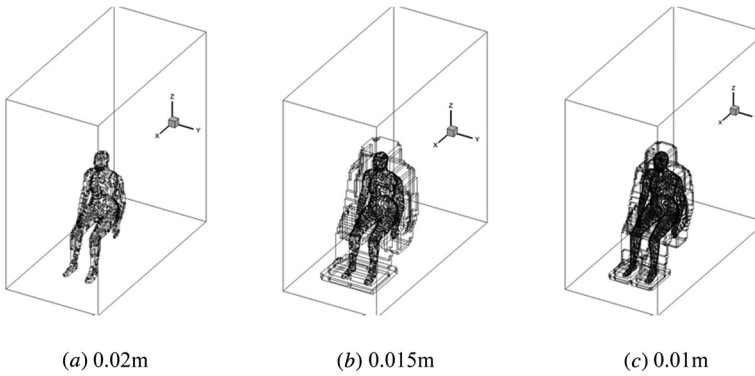


Figure 4. Three investigated lattice size and distributions around the thermal manikins.

3.2. MRT LBM simulation setup

The simulation applied D3Q19 model for the flow field, D3Q7 model for the thermal field, CBB for the boundary condition and WALE for the turbulence model to resolve the MRT lattice Boltzmann equation.

The velocity inlet had a velocity magnitude of 0.2 m/s and air temperature of 295.15 K. The outlet was set as pressure outlet with a gauge pressure of zero Pa. The surface temperature of the thermal manikin was uniformly distributed as the same as the experiment. The heat flux through the manikin surface was 38 W. The gravity was set to -9.8 m/s^2 in vertical direction as seen in Figure 3. The natural convection was modeling by the Boussinesq assumption, which is appropriate when the temperature difference at the boundary is small. The enhanced wall function was applied for the near wall treatment in the WLES, which considered the effect of pressure gradients was valid for all wall y^+ [33].

Three lattice sizes and distributions have varied total number of lattices. In this study, we proposed three lattice distributions as shown in Figure 4. Figure 4(a) applied a uniform lattice size of 0.02 m yielded 0.9 million total number of lattices. However, the boundaries surrounding the

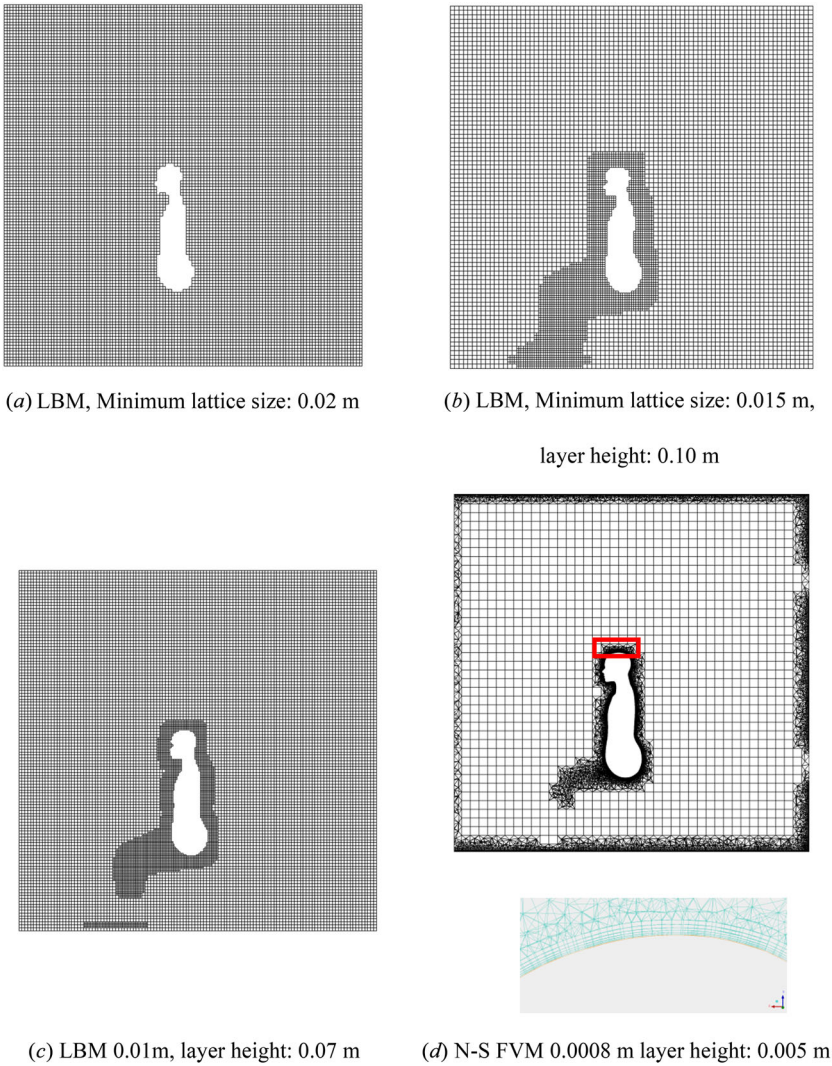


Figure 5. Three lattice distributions in MRT LBM (*a*, *b*, and *c*) and mesh distribution in N-S FVM (*d*).

manikin geometry was ambiguous. This may cause numerical errors because the surrounding lattice may occupy some solid space in the manikin body. Hence, the fluid space may become larger than reality in the simulation. In order to address the errors, as seen in Figure 4 (*b*), we applied the hybrid lattices that defined the lattice size adjacent to the manikin, at the boundary layer and far-fluid field as 0.015 m and 0.03 m, respectively [34]. This yielded the minimum total number of lattices about 0.36 million. The lattice distribution in Figure 4c was further improved by replacing the lattice size adjacent to the boundary from 0.01 m to 0.02 m. Figure 5b presented a closer look of the lattice distribution. As seen in Figures 4c and 5c, the lattice around the manikin became denser and the joint surface became smoother.

The simulation was conducted in transient iterations. We iterated the case for the first 50 seconds to get a stable airflow conditions and then another 50 seconds to acquire the averaged data.

3.3. Finite volume method (FVM) setup

In this study, FVM was applied to resolve the N-S equation referred to previous studies by [7-8, 26, 29]. In order to compare with the MRT LBM, this article applied similar turbulence model as

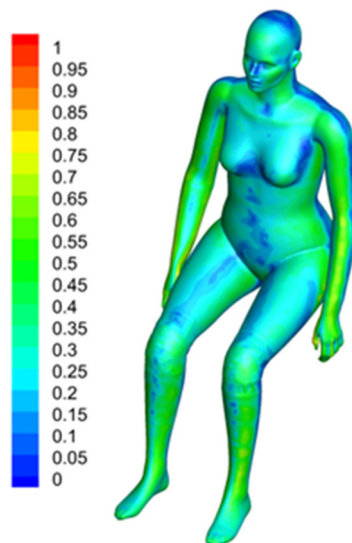


Figure 6. Distribution of wall y^+ around the manikin surface in FVM.

LES. We applied enhanced wall function as near wall treatment by condensing the lattices close to the wall and manikins to guarantee the wall y^+ was less than 1. The yielding minimum mesh size near the manikins was 0.8 mm. To reduce the number of grids, we applied prism and hexahedron meshes at the boundary layer. As seen in Figure 4d, there were six layers of prism meshes adjacent to the manikin surfaces with a minimum resolution of 0.3 mm.

The pressure–velocity coupling scheme was set as SIMPLEC. The spatial discretization applied the least squares cell based and the momentum terms were modeled by bounded central differencing scheme. The simulation results were analyzed by the same method as the MRT LBM. Figure 6 showed the yielded wall y^+ surrounding the manikin surface. It appeared that the wall y^+ distribution is uneven at the body surfaces. Wall y^+ is large at the surfaces with large shear stress. The parallel airflow velocities would lead to higher shear stress and thus yielded higher Wall y^+ . Figure 6 showed that all wall y^+ was less than one, indicted the mesh size was small enough for the near wall treatment in the LES model.

4. Results and discussion

In order to see the predication accuracy of the simulation methods, we compared the experiment and simulation data of four lattice distributions in nine vertical lines [31].

4.1. Airflow field

Figure 7 showed velocity contours in four cases at the middle plane of the computational domain. As shown in Figure 7, without obstruction, the velocity field in the upper area of the manikin was similar. Two high-velocity regions existed on the back wall. Four cases had similar results at the outlets. In the flow region beneath the manikin, the airflow in LBM 0.01 m case was similar with the N-S FVM case but not with other cases. In the LBM 0.01 m and FVM, we condensed the mesh in the region beneath the legs so that the mesh quality was proper in the region. The velocity distribution varied in the other two cases where the lattice distribution may be too coarse to cause the numerical error. The lattice size in that region beneath the leg should be less than 0.015 m.

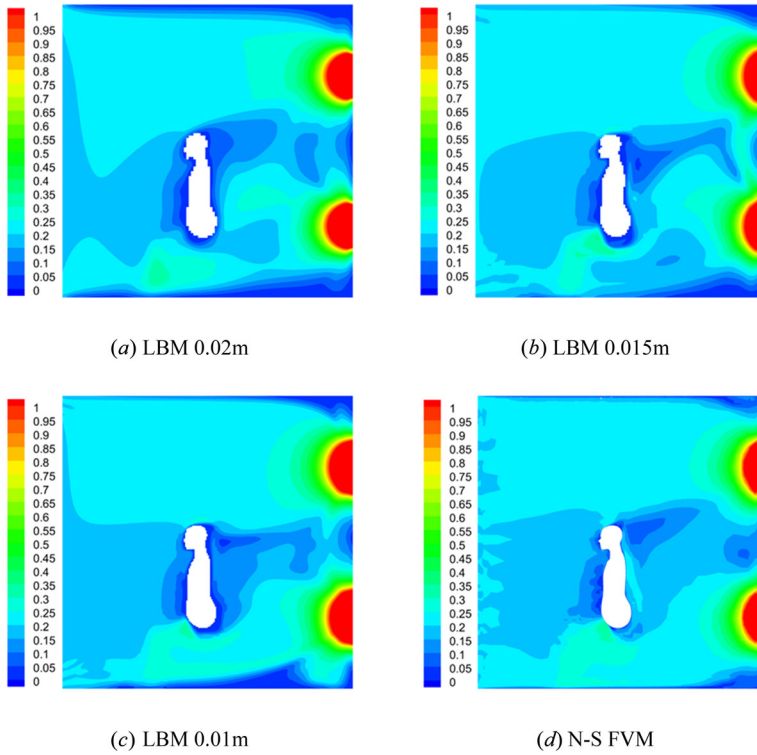


Figure 7. Simulated airflow field in the middle cross-section plane of the ventilated room. Unit: m/s.

Low-velocity region existed near the floor and the ceiling in three MRT LBM cases. However, in N-S FVM case, this low-velocity region was not obvious. This indicated that the MRT LBM and FVM had different performance in predicting the airflow adjacent to ceiling and floor.

There was a low-velocity region in front of the thermal manikin in all four cases. This low-velocity region extended to the inlet opening. However, the four cases showed varied velocity distribution in the front and behind the manikins. Behind the manikins, a low-velocity region existed and extended to the back wall. In the cases of LBM 0.015 m and 0.01 m, the velocities behind the manikins were obviously lower than the LBM 0.01 m and FVM. FVM yielded an averaged velocity up to 0.2 m/s while MRT LBM lower than 0.2 m/s. Comparing the three cases of LBM, we can see the velocity region close to the behind wall behind the manikin varied. The LBM 0.01 m agreed well with the FVM in that region.

In order to understand the airflow patterns, Figure 8 presented the streamlines of velocity in the middle cross-section plane under LBM 0.01 m case. In front of the manikin, the airflow separated into two branches. One branch went to the upper outlet and the other to the lower outlet. This led to a high turbulent and low-velocity region behind the manikin. We also noticed a weak thermal plume existed behinds the manikin due to the buoyancy effect from the thermal manikin surface.

Figure 9 showed the temperature contours of four cases at the middle cross-section plane of the computational domain. As shown in Figure 9, there was a vertical thermal plume behind the manikin due to the buoyancy effect from the thermal manikin surface. The temperature distribution behind the manikin in LBM 0.01m was comparable with the FVM than LBM 0.02m and LBM 0.015m. Besides, the condensed lattice distribution yielded precise prediction of the thermal fields. Because there was lack of experimental data on the temperature field, we cannot validate the simulated thermal fields in this study.

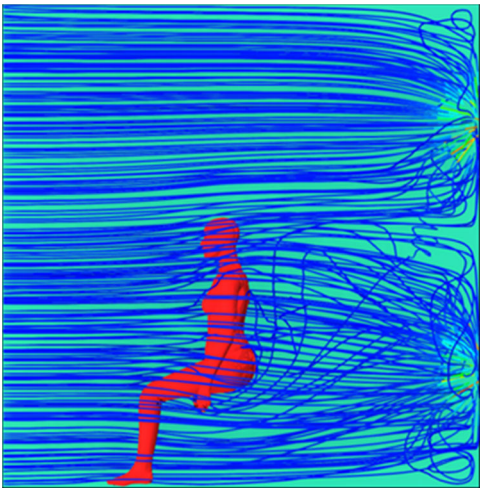


Figure 8. Streamlines of airflow in the middle cross-section plane under the LBM 0.01 m case. Unit: m/s.

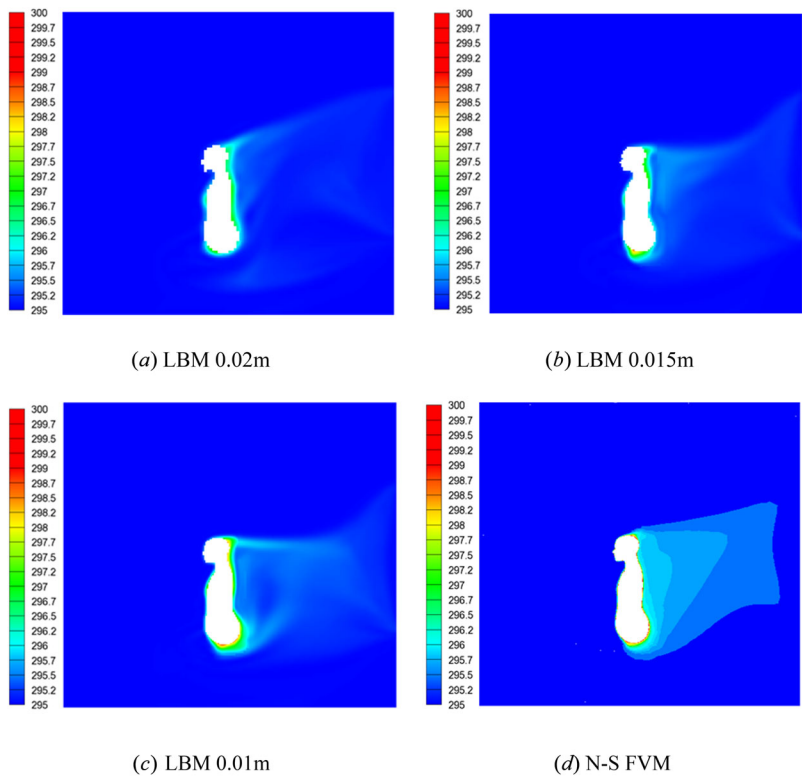


Figure 9. contours of airflow field in the middle cross-section plane. Unit: m/s.

In order to know the prediction accuracy, Figure 10 presented the comparison of velocity magnitude in the sample lines close to the inlet (Line 1, 4 and 7). In all four cases, the velocity in the flow region was quite similar, presented a uniform distribution. In Figure 7, we can also see a large difference of velocity contours in front of the manikins. This indicated that the simulation results were very sensitive to the lattice distribution.

The simulated results were quite different from the experiment data [31]. The simulation set a uniform distribution of inlet velocity speed at 0.2 m/s, which was calculated by the measured total

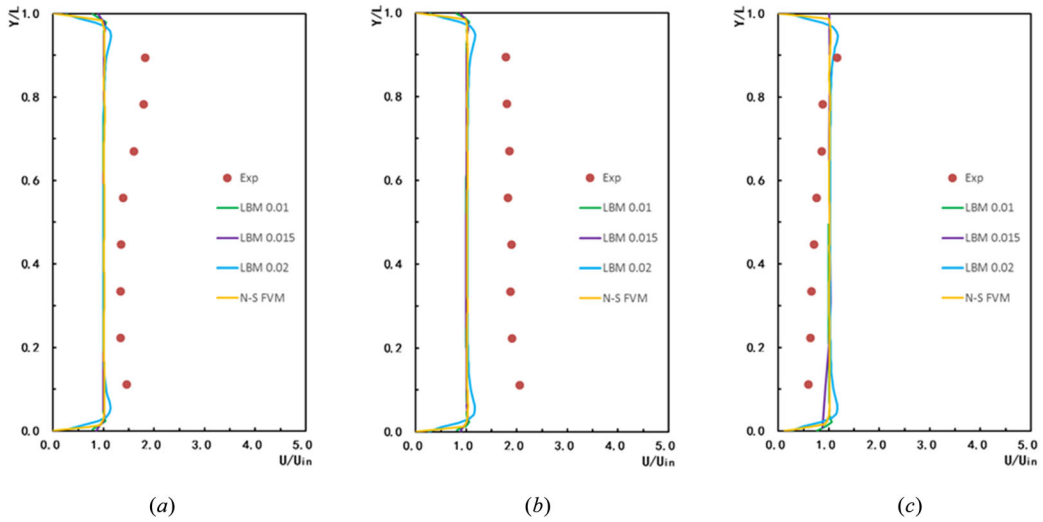


Figure 10. Validation of velocity fields in front of manikin in Line 1 (a), Line 4 (b), and Line 7 (c).

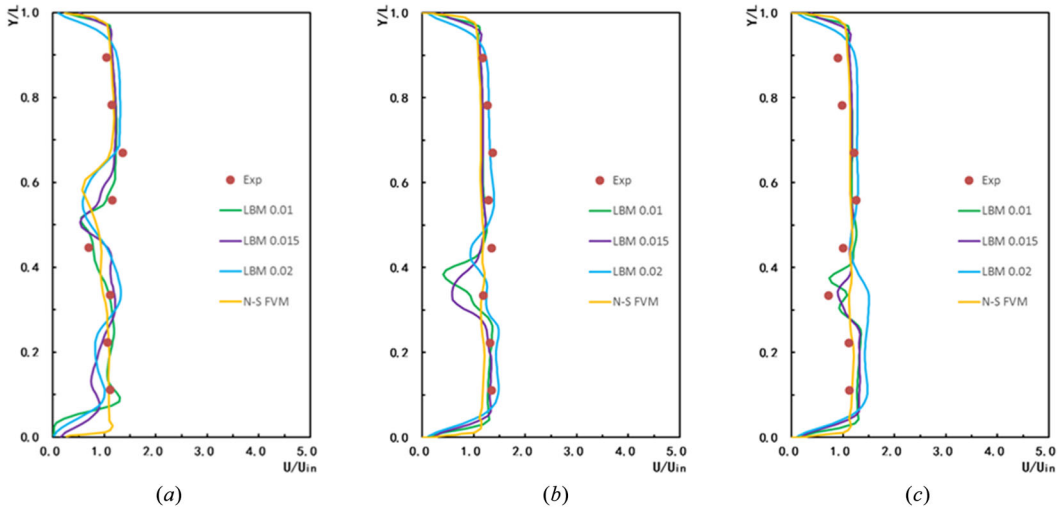


Figure 11. Validation of velocity field behind the manikin in Line 2 (a), Line 5 (b), and Line 8 (c).

flow rate at the outlets divided by the inlet opening area. However, in the experiment, the inlet velocity was rather difficult to be uniformly distributed as seen in Figure 10 because of the outside air may influence it.

Figure 11 is the comparison of velocity magnitude in the flow region behind the thermal manikin. As shown in Figure 11a, the LBM 0.01 m case had the optimal overall agreement with the experiment data. The LBM 0.015 m case achieved less overall agreement but better than LBM 0.02 m.

Line 2 was the sampling line behind the manikin in the middle cross-section plane. From the results, the simulated velocity by FVM behind the manikin head ($Y/L = 0.55$) was a little lower than the experiment data. The LBM 0.015 m and 0.01 m had good performance while LBM 0.02 m case was the worst in the flow region behind the manikin. The FVM had its disadvantage in predicting the airflow distribution in this flow region. MRT LBM had an advantage in predicting the velocity field, however, the lattice size should better be less than 0.015 m.

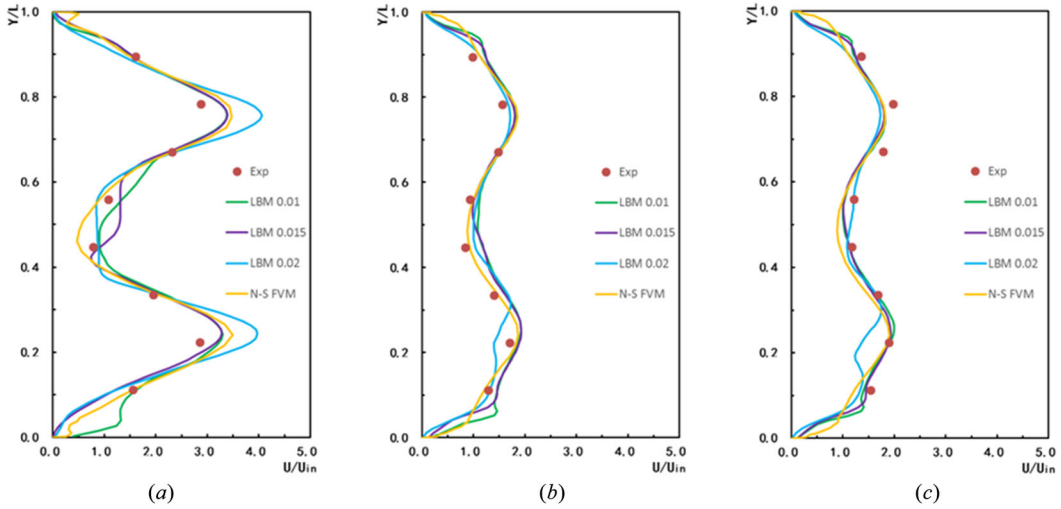


Figure 12. Validation of velocity field in Line 3 (a), Line 6 (b), and Line 9 (c).

Lines 5 and 8 were the sampling lines behind the manikin. As shown in Figure 11b,c, we found a low-velocity region behind the hands of the manikin ($Y/L = 0.35$). As shown in Figure 10b,c, the simulated velocity by LBM 0.01 m and 0.015 m behind the manikin hand ($Y/L = 0.35$) was a little lower than the experiment data, while the N-S FVM did not succeed to predict the low-velocity region behind the hand of manikin. As shown in Figure 11c, the LBM 0.01 m case had the optimal overall agreement with the experiment data. The result in LBM 0.015 m case was also acceptable, while an obvious error had occurred in LBM 0.02 m case.

Figure 12 showed the comparison of velocity magnitude in the sample lines close to the outlet (lines 3, 6 and 9). Line 2 was the sampling line between the manikin and back wall in the middle plane. From the results, LBM 0.01m case showed the best agreement with experiment data. The simulated velocity by LBM 0.02 m at $Y/L = 0.25$ and 0.75 was a little higher than the experiment data. However, N-S FVM at $Y/L = 0.5$ was a little lower than the experiment data. From the results shown in Figure 7, we can see the area of low-velocity region behind the manikin predicted by the LBM 0.01m was larger than the FVM. As shown in Figure 12b,c, the LBM 0.01m and 0.015m and N-S FVM case had the best agreement with the experiment data. MRT LBM and N-S FVM both can predict the velocity field, however, in MRT LBM, the lattice size should better be less than 0.015 m.

4.2. Comparison of computation time

We used Normalized Root-Mean-Square Deviation (NRMSD) to quantify the prediction accuracy. Its formula was as bellows:

$$\text{RMSD} = \sqrt{\frac{\sum_{i=1}^n (\hat{y}_i - y_i)^2}{n}}$$

$$\text{NRMSD} = \frac{\text{RMSD}}{\bar{y}}$$

where \hat{y}_i is predicted values, y_i is regression's dependent variable, and \bar{y} is averaged value of predicted variable.

In order to evaluate the prediction accuracy, Table 1 presented the overall accuracy of MRT LBM and FVM cases. Due to the discrepancy between simulated inlet air velocity and the

Table 1. Prediction accuracy of MRT LBM and FVM cases in all lines. Unit: %.

Sampling lines	0.01 m	0.015m	0.02 m	FVM
Line 1	—	—	—	—
Line 2	8.92	20.23	26.04	19.98
Line 3	13.78	12.83	26.82	15.96
Line 4	—	—	—	—
Line 5	10.57	18.56	13.00	10.95
Line 6	9.95	10.56	16.81	13.24
Line 7	—	—	—	—
Line 8	20.00	16.52	35.38	17.98
Line 9	17.03	16.47	14.39	9.81
Averaged accuracy	13.38	15.86	22.07	14.65

Table 2. Comparison of these four cases in grids number and computation time.

Case	Grid size (m)	Grid number (Million)	Computation time (Hour)	Accuracy (Average of NRMSD)
LBM 0.02m	0.02	0.9	8	22.07%
LBM 0.015 m	0.015–0.03	0.36	3.5	15.86%
LBM 0.01 m	0.01–0.02	1.1	21	13.38%
N-S FVM	0.0003–0.08	3.8	124	14.65%

measurement as mentioned above, we did not analyze the prediction accuracy in three lines at line 1, 4 and 7. In terms of line 2 and line 3, the accuracy of LBM 0.02 m was the worst. The accuracy of LBM 0.01 m was better than FVM. Besides, LBM 0.01 m case had the best prediction accuracy in the flow region behind the manikin.

Theoretically, the velocity in line 5 and line 8 should be the same and have similar accuracy. However, the predicted results showed that the accuracy has a large difference between line 5 and line 8, similarly as the line 6 and line 9. This may because in the experiment, even though the geometry was perfectly symmetric distributed, but the velocity field was not. We also noticed that LBM had different predicted accuracy in different lines. The LBM model required further optimization in several flow regions such as at line 3.

The comparison of grid number and computation time of four cases was presented in Table 2. The LBM 0.02 m case used the uniform lattices of 0.02 m. The computation time was up to 8 hours but the predicted results were not the optimal. Compared to LBM 0.02 m, the grid number in LBM 0.01 m only increased by 0.2 million because the hybrid lattices were used. Among three LBM cases, the LBM 0.015 m used the minimal grid number, which applied the hybrid lattices adjacent to the manikin. Because of the minimum grid number, the computation time as well as the memory occupancy was the minimum in three LBM cases. Although LBM 0.01 m took the longest computation time, its prediction accuracy was less than 14%. There was a tradeoff of time and prediction accuracy in LBM. The hybrid lattice and the proper lattice minimum size were the critical factors when conducting LBM simulations.

The N-S FVM case took the longest computation time. The time was up to 124 h, almost 6 times of the LBM 0.01 m case. This is mainly due to the large surface grid size in FVM because LES requires very tiny grid sizes at the boundaries. The smaller the grid size yielded a larger grid number and a longer computation time. The computation time of LBM 0.01 m was only one-sixth of FVM without sacrificing the prediction accuracy.

5. Conclusion

In this study, we conducted several CFD simulations of the airflow and thermal fields surrounding the thermal manikins using multiple-relaxation-time Lattice Boltzmann method (MRT-LBM) and finite volume methods (FVM) with large eddy simulation method. We also validated the CFD simulation results based on the experimental data. Based on the analysis, we analyzed the

factors that influenced the computation time and prediction accuracy of CFD simulation, such as grid size and distribution. Several conclusions were summarized as follows:

- a. The prediction accuracy of MRT-LBM method was highly depended on the lattice distribution. In MRT-LBM, the lattice size of 0.02m yielded a prediction accuracy of 22.07% on the airflow field. The hybrid lattice distribution can yield higher accuracy up to 13.68%. The proper hybrid lattice distribution had the lattice size: adjacent to the manikins 0.01 m and far field 0.02m. The overall performance of MRT-LBM with hybrid lattice was superior to the traditional FVM.
- b. The computation time of MRT-LBM was only one-sixth of that of FVM method with similar prediction accuracy.
- c. The simulated thermal field was similar between FVM and MRT LBM with the lattice size 0.01m. However, because we could not find the measured data, we cannot compare the prediction accuracy of thermal fields. Besides, in order to couple with more complicate cases, we will investigate MRT LBM methods in condition with complex indoor air distribution.

Funding

The research in this article was supported by the National Key R&D Program of the Ministry of Science and Technology, China, on “Green Buildings and Building Industrialization” through Grant No. 2018YFC0705300. We also thank the financial support from the Natural Science Foundation of Tianjin (Grant No. 19JCQNJC07100).

References

- [1] P. Wargocki, *et al.*, “Perceived air quality, sick building syndrome (SBS) symptoms and productivity in an office with two different pollution loads,” *Indoor Air*, vol. 9, no. 3, pp. 165, 1999. DOI: [10.1111/j.1600-0668.1999.t01-1-00003.x](https://doi.org/10.1111/j.1600-0668.1999.t01-1-00003.x).
- [2] D. Zukowska, A. Melikov, and Z. Popiolek, “Impact of personal factors and furniture arrangement on the thermal plume above a sitting occupant,” *Build. Environ.*, vol. 49, no. 3, pp. 104–116, 2012. DOI: [10.1016/j.buildenv.2011.09.015](https://doi.org/10.1016/j.buildenv.2011.09.015).
- [3] N. P. Gao, and J. L. Niu, “CFD Study of the thermal environment around a human body: a review,” *Indoor Built Environment*, vol. 14, no. 1, pp. 5–16, 2005. DOI: [10.1177/1420326X05050132](https://doi.org/10.1177/1420326X05050132).
- [4] P. O. Fanger, *et al.*, “Comfort limits for asymmetric thermal radiation,” *Energy Build.*, vol. 8, no. 3, pp. 225–236, 1985. DOI: [10.1016/0378-7788\(85\)90006-4](https://doi.org/10.1016/0378-7788(85)90006-4).
- [5] D. Licina, *et al.*, “Experimental investigation of the human convective boundary layer in a quiescent indoor environment,” *Build. Environ.*, vol. 75, no. 1, pp. 79–91, 2014. DOI: [10.1016/j.buildenv.2014.01.016](https://doi.org/10.1016/j.buildenv.2014.01.016).
- [6] N. Gao, and J. Niu, “CFD study on micro-environment around human body and personalized ventilation,” *Build. Environ.*, vol. 39, no. 7, pp. 795–805, 2004. DOI: [10.1016/j.buildenv.2004.01.026](https://doi.org/10.1016/j.buildenv.2004.01.026).
- [7] C. Topp, P. V. Nielsen, and D. N. Sørensen, “Application of computer simulated persons in indoor environmental modeling,” *ASHRAE trans.*, vol. 108, no. 2, pp. 1084–1089, 2002.
- [8] C. Topp, “Influence of geometry of a computer simulated person on contaminant distribution and personal exposure,” *Roomvent*, vol. 1, pp. 265–268, 2002.
- [9] S. A. Keshavarz, M. Salmanzadeh, and G. Ahmadi, “Computational modeling of time resolved exposure level analysis of a heated breathing manikin with rotation in a room,” *J. Aerosol sci.*, vol. 103, pp. 117–131, 2017. DOI: [10.1016/j.jaerosci.2016.09.005](https://doi.org/10.1016/j.jaerosci.2016.09.005).
- [10] N. Martinho, A. Lopes, and M. G. D. Silva, “Evaluation of errors on the CFD computation of air flow and heat transfer around the human body,” *Building Environment*, vol. 58, pp. 58–69, 2012. DOI: [10.1016/j.buildenv.2012.06.018](https://doi.org/10.1016/j.buildenv.2012.06.018).
- [11] J. M. Yeomans, “Mesoscale simulations lattice Boltzmann and particle algorithms,” *Phys. A*, vol. 369, no. 1, pp. 159–184, 2006. DOI: [10.1016/j.physa.2006.04.011](https://doi.org/10.1016/j.physa.2006.04.011).
- [12] Z. Li, M. Yang, and Y. Zhang, “Numerical simulation of melting problems using the lattice Boltzmann method with the interfacial tracking method,” *Numerical Heat Transfer, Part A: Applicat.*, vol. 68, no. 11, pp. 1175–1197, 2015. DOI: [10.1080/10407782.2015.1037126](https://doi.org/10.1080/10407782.2015.1037126).

- [13] M. Hussain, and W.-Q. Tao, "Numerical prediction of effective thermal conductivity of ceramic fiber board using lattice Boltzmann method," *Numer. Heat Transf., A: Appl.*, vol. 74, no. 6, pp. 1285–1300, 2018. DOI: [10.1080/10407782.2018.1523599](https://doi.org/10.1080/10407782.2018.1523599).
- [14] Q. Ren, and C. L. Chan, "Numerical simulation of a 2D electrothermal pump by lattice Boltzmann method on GPU," *Numer. Heat Transf., A: Appl.*, vol. 69, no. 7, pp. 677–693, 2016. DOI: [10.1080/10407782.2015.1090826](https://doi.org/10.1080/10407782.2015.1090826).
- [15] S. Nataraj, K. S. Reddy, and S. P. Thampi, "Lattice Boltzmann simulations of a radiatively participating fluid in Rayleigh–Benard convection," *Numer. Heat Transf., A: Appl.*, vol. 72, no. 4, pp. 313–329, 2017. DOI: [10.1080/10407782.2017.1376936](https://doi.org/10.1080/10407782.2017.1376936).
- [16] S. Chen, and G. D. Doolen, "Lattice Boltzmann method for fluid flows," *annu. rev. Fluid Mechanics*, vol. 30, no. 1, pp. 329–364, 1998. DOI: [10.1146/annurev.fluid.30.1.329](https://doi.org/10.1146/annurev.fluid.30.1.329).
- [17] X. He, and L. S. Luo, "A priori derivation of the lattice Boltzmann equation," *Phys. Rev. E*, vol. 55, no. 6, pp. R6333–R6336, 1997. DOI: [10.1103/PhysRevE.55.R6333](https://doi.org/10.1103/PhysRevE.55.R6333).
- [18] J. Lätt, B. Chopard, S. Succi, and F. Toschi, "Numerical analysis of the averaged flow field in a turbulent lattice Boltzmann simulation," *Physica A*, vol. 362, no. 1, pp. 6–10, 2006. DOI: [10.1016/j.physa.2005.09.016](https://doi.org/10.1016/j.physa.2005.09.016).
- [19] H. Yu, L.-S. Luo, and S. S. Girimaji, "LES of turbulent square jet flow using an MRT lattice Boltzmann model," *Comput. Fluids*, vol. 35, no. 8-9, pp. 957–965, 2006. DOI: [10.1016/j.compfluid.2005.04.009](https://doi.org/10.1016/j.compfluid.2005.04.009).
- [20] Y. Qian, D. d'Humières, and P. Lallemand, "Lattice BGK models for Navier–Stokes equation," *Europhys. Lett*, vol. 17, no. 6, pp. 479–484, 1992. DOI: [10.1209/0295-5075/17/6/001](https://doi.org/10.1209/0295-5075/17/6/001).
- [21] P. Lallemand, and L.-S. Luo, "Theory of the lattice Boltzmann method: dispersion, dissipation, isotropy, Galilean invariance and stability," *Phys. Rev. E*, vol. 61, no. 6, pp. 6546–6562, 2000. DOI: [10.1103/PhysRevE.61.6546](https://doi.org/10.1103/PhysRevE.61.6546).
- [22] Y. Chen, H. Ohashi, and M. Akiyama, "Thermal lattice Bhatnagar-Gross-Krook model without nonlinear deviations in macrodynamic equations," *Phys. Rev. E Statist. Phys. Plasmas Fluids Related Interdiscip Top.*, vol. 50, no. 4, pp. 2776, 1994. DOI: [10.1103/PhysRevE.50.2776](https://doi.org/10.1103/PhysRevE.50.2776).
- [23] P. Lallemand, and L. S. Luo, "Theory of the lattice Boltzmann method: Acoustic and thermal properties in two and three dimensions," *Physical Rev. E Statist. Nonlinear Soft Matter Phys.*, vol. 68, no. 2, pp. 036706, 2003. DOI: [10.1103/PhysRevE.68.036706](https://doi.org/10.1103/PhysRevE.68.036706).
- [24] Z. Guo, B. Shi, and C. Zheng, "A coupled lattice BGK model for the Boussinesq equations," *Int. J. Numer. Methods Fluids*, vol. 39, no. 4, pp. 325–342, 2002. DOI: [10.1002/fld.337](https://doi.org/10.1002/fld.337).
- [25] G. I. D'Humières, *et al.*, "Multiple-relaxation-time lattice Boltzmann models in three dimensions," *Philosoph. Trans.*, vol. 360, no. 1792, pp. 437, 2002. DOI: [10.1098/rsta.2001.0955](https://doi.org/10.1098/rsta.2001.0955).
- [26] H. Yoshida, and M. Nagaoka, "Multiple-relaxation-time lattice Boltzmann model for the convection and anisotropic diffusion equation," *Comput. Phys.*, vol. 229, no. 20, pp. 7774–7795, 2010. DOI: [10.1016/j.jcp.2010.06.037](https://doi.org/10.1016/j.jcp.2010.06.037).
- [27] F. Ducros, F. Nicoud, and T. Poinso, "Wall-adapting local Eddy-viscosity models simulations complex geometries," *Numer. Methods Fluid Dyn.*, pp. 293–300, 1998.
- [28] R. Verberg, and A. J. Ladd, "Accuracy and stability of a lattice-Boltzmann model with subgrid scale boundary conditions.[J]," *Phys. Rev. E Statist. Nonlinear Soft Matter Phys.*, vol. 65, pp. 2–016701, 2002. (DOI: [10.1103/PhysRevE.65.016701](https://doi.org/10.1103/PhysRevE.65.016701)).
- [29] R. Verberg, and A. J. C. Ladd, "Ladd Lattice-Boltzmann Model with Sub-Grid-Scale Boundary Conditions," *Phys. Rev. Lett*, vol. 84, no. 10, pp. 2148, 2000.
- [30] Y. Yan, *et al.*, "Evaluation of manikin simplification methods for CFD simulations in occupied indoor environments," *Energy Build.*, vol. 127, pp. 611–626, 2016. DOI: [10.1016/j.enbuild.2016.06.030](https://doi.org/10.1016/j.enbuild.2016.06.030).
- [31] P. V. Nielsen, "Benchmarks test for a computer simulated person," *Indoor Air*, vol. 14, no. 7, pp. 144–156, 2003.
- [32] N. S. Dan, and L. K. Voigt, "Modeling flow and heat transfer around a seated human body by computational dynamics," *Build. Environ.*, vol. 38, no. 6, pp. 753–762, 2003. DOI: [10.1016/S0360-1323\(03\)00027-1](https://doi.org/10.1016/S0360-1323(03)00027-1).
- [33] T. H. Shih, L. A. Povinelli, N. S. Liu, M. G. Potapczuk, and J. L. Lumley, (1999). "A generalized wall function," NASA Technical Report, NASA Glenn Research Center, Cleveland, OH.
- [34] D. Yu, R. Mei, and S. Wei, "A multi-block lattice boltzmann method for viscous fluid flows," *Int. J. Numer. Methods Fluids*, vol. 39, no. 2, pp. 99–120, 2002. DOI: [10.1002/fld.280](https://doi.org/10.1002/fld.280).